Tribol Lett (2015) 59:5
DOI 10.1007/s11249-015-0525-2

ORIGINAL PAPER

Crack Healing Between Rough Polycrystalline Silicon Hydrophilic Surfaces in *n*-Pentanol and Water Vapors

Emrecan Soylemez[1] · **Maarten P. de Boer**[1]

Received: 16 February 2015 / Accepted: 2 April 2015 / Published online: 22 May 2015

Abstract The crack healing rates of polycrystalline silicon microcantilevers in contact with a substrate are measured in *n*-pentanol vapor at different partial pressures, p/p_s. The absolute value of the slope of the logarithmic average crack healing velocity $\bar{v}$ versus the energy release rate G, $|d[\log(\bar{v})]/dG|$, is constant and decreases with increasing p/p_s. The slope dependence on p/p_s is equivalent to that in a water vapor environment. This slope is independent of p/p_s in glass stress corrosion cracking experiments due to chemical kinetics, while the present experiments reflect a capillary bridge nucleation mechanism across nanometer-scale gaps created by surface roughness. Equilibrium measurements of adhesion versus p/p_s are also compared for *n*-pentanol and water vapor. For $p/p_s \leq 0.5$, adhesion is comparable for the two vapors, while for $p/p_s > 0.5$, adhesion in water vapor is approximately twice that in *n*-pentanol vapor. At lower p/p_s, this is explained by the larger Kelvin radius and the larger adsorbed layer thickness of *n*-pentanol. This combination enables larger asperity gaps to be bridged by capillary liquids. At higher p/p_s, adhesion in water vapor is larger because the work of adhesion of capillary bridges becomes twice that of *n*-pentanol.

Keywords Capillary bridge nucleation · Crack healing · Adhesion · Lubrication · Alcohol

✉ Maarten P. de Boer
mpdebo@andrew.cmu.edu

[1] Mechanical Engineering Department, Carnegie Mellon University, Pittsburgh, PA 15213, USA

1 Introduction

Adhesion and friction due to surface forces constitute important performance and reliability concerns at the micro- and nanoscales [1–5]. Alcohol vapors that condense into lubricious oligomers [6, 7] or simply an adsorbed lubricant layer [8] have recently been proposed as a means to eliminate wear between rubbing surfaces in polycrystalline silicon (polysilicon) micromachined surfaces. While the vapors provide a highly beneficial effect, liquid bridges may condense in the interface and the associated capillary forces may cause the contacting surfaces to adhere, thwarting rubbing motion. Therefore, it is important to gain insight into factors that influence the conditions under which this proposed solution will operate. These include the vapor partial pressure, the surface roughness and the temperature. The understanding gained may also be relevant to commercial microelectromechanical system (MEMS) products such as digital mirror devices and interferometric modulator displays [9] in which capillary action can potentially affect operation.

Polysilicon can be considered to be a technical ceramic. With respect to adhesion, it is well known that slow crack propagation and crack healing occur in ceramic materials due to environmental effects under subcritical loading conditions. Many experiments have been conducted in controlled environments to understand these phenomena by presenting the data in the form of velocity (v) curves versus energy release rate (G) or stress intensity (K) [10]. Double cantilever beam (DCB) and double-cleavage drilled compression (DCDC) specimens have typically been utilized in the experiments [11].

Subcritical crack *propagation* has been observed in mica [12] and soda lime silica [13] at different relative humidity (RH) levels and in liquid water. In dry environment, cracks

propagate at the critical energy release rate, G_c. In a vapor environment, for a given value of $G < G_c$, the crack velocity increases as the RH level increases. Water vapor molecules or adsorbed liquid molecules react with strained Si–O–Si bonds at the crack tip and break the bonds to form silanol groups [10, 11]. Reactions are enhanced by increasing the RH and the stress, which leads to higher crack velocities. In addition to water, various alcohols, such as butyl, amyl, hexyl, heptyl, octyl, decyl and ethyl, have been investigated [13]. The subcritical crack propagation-driving mechanism was still attributed to the presence of water due to its high solubility in alcohols [11]. However, the alcohol chain length increment caused a small crack velocity decline [13]. In liquid water, cracks propagate at even lower energy release rates [13]. Capillary condensation, observed by atomic force microscope (AFM) phase imaging, has been directly associated with subcritical crack propagation under applied load [14].

Cracks also tend to *heal* under various conditions. One common method to induce crack healing is simply by unloading a specimen. Healed interfaces have then been studied to understand crack behavior upon re-propagation [12, 15]. Healing also occurs due to thermal annealing in humid environments, which creates pinch offs [16] or forms a ceramic gel structure in the interface [17]. Also, cracks created by a Vickers hardness test in fluoride glass healed at room temperature under humid conditions by a corrosion deposition mechanism at the crack tip [18]. The final states of the cracks at room temperature in [18] were independent of the RH levels. However, RH levels affected the kinetics of the healing mechanism.

One other mechanism to heal cracks is by capillary condensation, where liquid capillary bridges apply attractive forces to close cracks [19–21]. While subcritical crack propagation occurs in humid environments starting at min $G = \sim 200$ (mJ/m^2) [10], crack healing due to capillary adhesion is limited to $G \leq 2\gamma_{LV}$ (146 mJ/m^2 for water). Hence, for the same environmental conditions, crack healing or propagation can be observed depending on the magnitude of the applied loads.

Experiments have recently been conducted to observe the influence of *water* capillary bridge kinetics on the crack healing rates of oxide-coated polysilicon microcantilevers with nanometer-scale surface roughness [20, 22]. In this paper, we measure the crack length of such microcantilevers as a function of time at fixed *n-pentanol* partial pressure. The water vapor content in the alcohol was suppressed through the use of molecular sieves. We plot the absolute value of the average crack healing velocity ($\bar{v}$) versus the energy release rate (G). We find that $|d[\log(\bar{v})]/dG|$ increases with partial pressure p/p_s, similar to water vapor [20]. Moreover, we compare the adhesion energy per unit area of water and *n*-pentanol in equilibrium as a function of p/p_s. It is observed that adhesion in *n*-pentanol and water vapor is equivalent for $p/p_s \leq 0.5$, while adhesion in water vapor is approximately twice as large for $p/p_s > 0.5$. This is explained by considering the work of adhesion contributions due to the capillary bridge and the adsorbed liquid layer for each substance as a function of p/p_s.

2 Experimental Procedure

A microcantilever in contact with a substrate [3, 23] can be considered as a fracture mechanics specimen analogous to the DCB specimen. For this work, polysilicon microcantilevers were fabricated at Sandia National Laboratories in the SUMMiT V^{TM} process [24] and then released by critical point drying at Carnegie Mellon University. As imaged by interferometry, twenty freestanding cantilevers of lengths from 1050 to 2000 μm in 50-μm increments were obtained from a given chip. As illustrated in Fig. 1a, the height of the step-up support post is $h = 1.8$ μm, the cantilever width is $w = 20$ μm, and the cantilever thickness is $t = 2.5$ μm.

The freestanding cantilevers were placed in a load lock chamber and O_2 plasma-treated such that they were fully wetted by water or the alcohol. Samples adhered to the substrate and assumed the *S*-shape as in Fig. 1b after pumping down the chamber for plasma cleaning, similar to

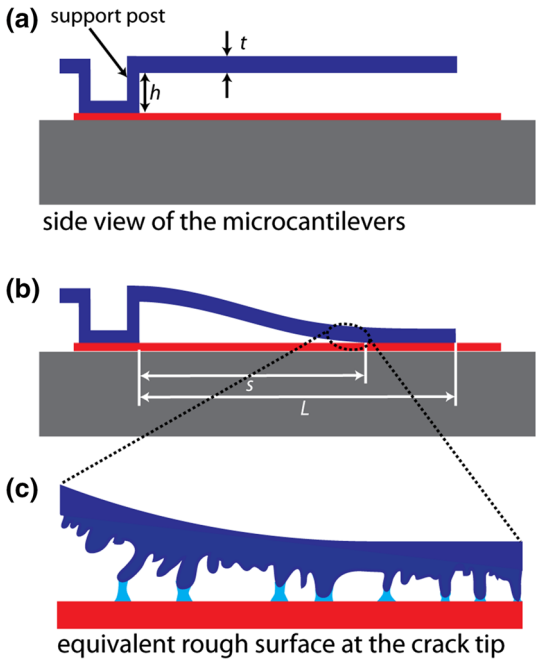

Fig. 1 Cross-sectional schematic geometry of the microcantilever **a** standing freely and **b** in the *S*-shape. **c** Equivalent rough surface schematic at the crack tip

[25]. After plasma cleaning, the sample was transferred to a main chamber under vacuum, which was then vented with dry high-purity (99.995 %) nitrogen. A viewport window in the main chamber enabled interferometric imaging of the microcantilevers [26]. Cantilevers were then in contact with the substrate beyond the crack tip at crack length s. The cantilever beam deflection is [27]

$$w(x) = h\left(\frac{x}{s}\right)^2\left(3 - \frac{2x}{s}\right), \quad (1)$$

which has the symmetrical "S"-shape.

It was previously shown that dry adhesion in these experiments is sensitive to the presence of particles intermittently produced by processing [28]. In the present work, spontaneous crack healing at low p/p_s (<0.5) correlated with the existence of low surface roughness ($\lesssim$2 nm root mean square (RMS)) and with low surface particle density. Having released, dried, and tested $\sim$40 chips, we summarize as follows. Cantilevers on chips with <2 nm RMS roughness and low surface particle density adhered to the substrate and assumed the S-shape while pumping down the chamber for plasma cleaning. Their adhesion generally increased at low p/p_s (<0.5). Cantilevers on chips with rougher surfaces or surfaces with only slightly higher particle densities did not adhere during the plasma clean and only exhibited spontaneous crack healing at higher p/p_s ($\geq$0.7). Crack healing was also previously reported only at higher $p/p_s \geq 0.7$, using samples of $\geq$2.7 nm RMS roughness [29]. The n-pentanol and water vapor samples reported below derive only from surfaces with <2 nm RMS roughness and low surface particle density. The case of ethanol vapor samples reported below is somewhat different, as will be explained in the discussion section.

Vapor was introduced, and partial pressure p/p_s was controlled by mixing dry and saturated vapor lines in a nitrogen carrier gas using ball-type gas flow meters and needle flow valves. Atmospheric water vapor is highly soluble in alcohol solvents. Furthermore, at room temperature, the vapor pressure of water, 22.3 mmHg, is significantly higher than n-pentanol, which has a vapor pressure of 1.9 mmHg. To minimize water content in the saturated N_2 line, we placed 3 Å molecular sieves into the n-pentanol fritted bubblers and waited 24 h prior to the experiment [30] to allow time for the water to be absorbed by the molecular sieves. Crack healing data were recorded after steady state p/p_s was attained, which occurred within $\sim$10 min after changing p/p_s to a new level [20]. A similar procedure was followed for ethanol.

Water vapor experiments were monitored by RH sensors (Vaisala models HMT334 and HMP234). However, alcohols corrode the Vaisala sensors. We tested a commercial chilled mirror hygrometer to monitor the p/p_s of n-pentanol. This technique is based on sensing reflected light from a stainless steel surface. In principle, a condensed liquid on the surface scatters light due to a high liquid contact angle, with the reduced intensity indicating the dew temperature. However, n-pentanol gave a low contact angle on stainless steel. We applied various coatings to increase the contact angle. This allowed flow calibration, but the coatings degraded quickly in longer experiments. The calibration data combined with experience from the water vapor RH control nonetheless enabled good p/p_s control for the alcohols.

According to Eq. (1), near the crack tip, the nominal separation between the counterfacing surfaces is less a few nanometers over a distance of many micrometers; this enables capillary bridge nucleation between opposing asperities in the counterfaces, as schematically represented in Fig. 1c. The p/p_s was increased to a desired level by increasing the ratio of saturated to dry nitrogen introduced into the chamber. For sufficiently high p/p_s, spontaneous crack healing was observed. This level was maintained until no further change was detected and then increased to a higher level. Phase-shifting interferometry [31] at 10-s intervals enabled determination of s versus time for up to 20 microcantilevers. With a 5X objective (NA = 0.14), s could be determined with $\pm$5.5 μm ($\pm$2 pixels) uncertainty. With Young's modulus E = 164 GPa [32], the energy release rate G (J/m^2) of a given cantilever was calculated according to [27]

$$G = \frac{3}{2}E\frac{h^2t^3}{s^4}. \quad (2)$$

3 Results

In equilibrium, $G = \Gamma$, the adhesion energy per unit area (equivalent to G_c above). The value of Γ in dry nitrogen was from 0.025 to 0.040 mJ/m^2 (s = 840–746 μm). These low values can be attributed to van der Waals forces and are typical of dry rough interfaces in MEMS [33]. The n-pentanol p/p_s first was increased to 0.3, and after 10 min, crack healing began. Eventually, healing occurred for 13 cantilevers out of 20. Examples are seen in Fig. 2a. Figure 2 plots the healing data for each p/p_s level, and each color represents the same cantilever throughout the figure. Here, G is calculated from the measured value of s and plotted against time. G is seen to increase from 0.02 to 0.04 to 0.03–0.08 mJ/m^2 over 250 min in Fig. 2a. The p/p_s was then increased to 0.5, and for some cantilevers, healing events started within 30 s. Crack healing continued for 1000 min. As seen in Fig. 2b, G increased further to 0.1–0.2 mJ/m^2. Again, 13 cantilevers responded to the p/p_s level; however, this time, some of the cantilevers that had healed at the previous p/p_s level did not heal, while some

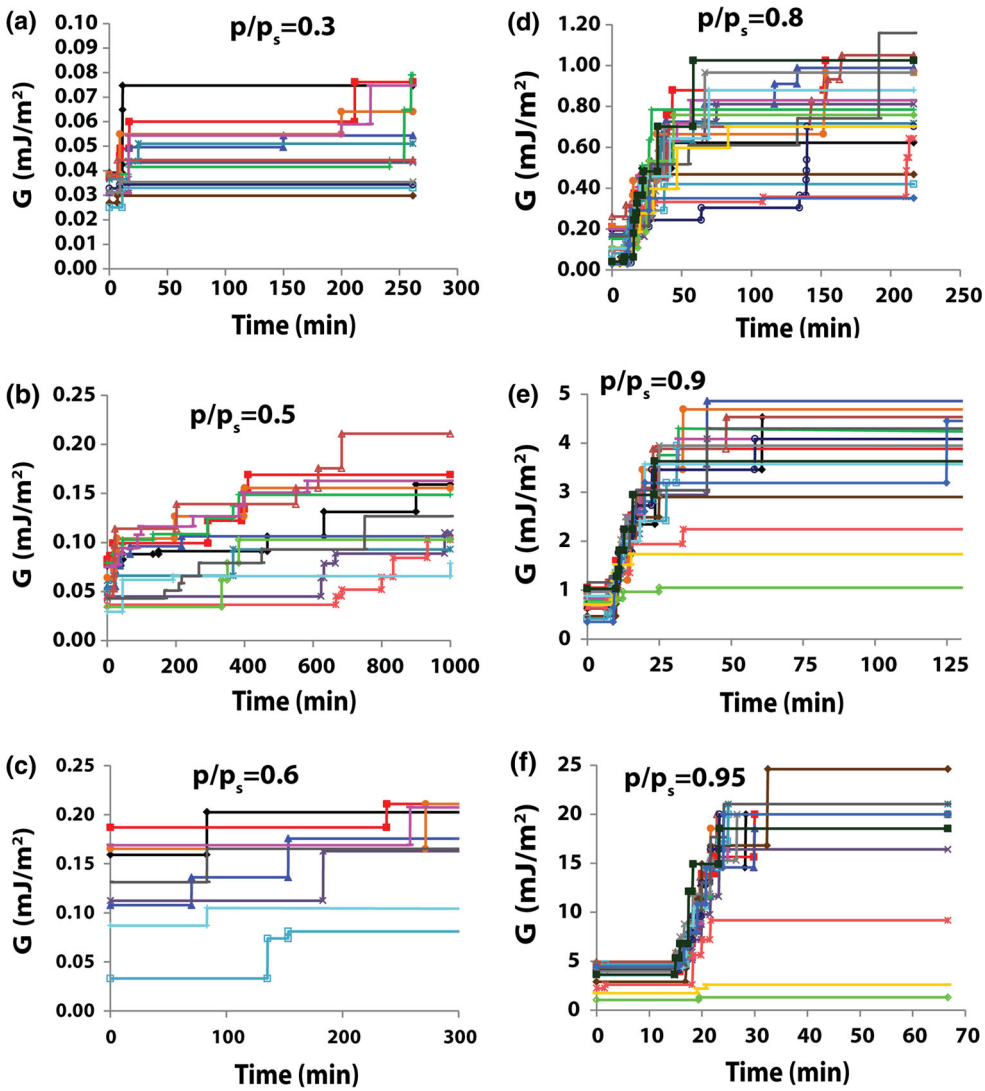

Fig. 2 Crack healing data over time for *n*-pentanol. *Colored lines* represent energy release rate G for different individual microcantilevers after increasing p/p_s from **a** 0 to 0.3, **b** 0.3 to 0.5, **c** 0.5 to 0.6, **d** 0.6 to 0.8, **e** 0.8 to 0.9 and **f** from 0.9 to 0.95. Colors are the same for the same microcantilevers at different p/p_s. Note that the *x*- and *y*-scales change in each plot (Color figure online)

previously nonresponsive cantilevers responded for the first time. A smaller increment to $p/p_s = 0.6$ leads to fewer cantilever responses as shown in Fig. 2c. With this step, most of the cantilevers reached $\sim$ 0.2 mJ/m^2. However, at this point, there were still cantilevers that had not healed since the beginning of the experiment. All of the cantilevers did heal in the next step at $p/p_s = 0.8$. Here, G increases to 0.3–1.1 mJ/m^2 over $\sim$200 min, as shown in Fig. 2d. At $p/p_s = 0.9$, G climbed to 1–5 mJ/m^2 over $\sim$60 min, as seen in Fig. 2e. Finally, at $p/p_s = 0.95$, G attained $\sim$20 mJ/m^2 in a much shorter time (35 min), as seen in Fig. 2f.

Next, the chamber was pumped to a medium vacuum level of $\sim$100 mTorr using a dry scroll pump for $\sim$230 min. Vibrations precluded interferometry during this period. However, after a nitrogen purge, the interferograms in Fig. 3 show that cracks propagated in dry conditions. Compared with the fully wet condition as seen in Fig. 3b, the crack lengths are substantially longer in Fig. 3c at $p/p_s = 0$. In our previous experiments in water vapor, cantilevers have always exhibited negligible crack propagation upon reducing RH. This may be because once the cracks heal, water molecules cause strong hydrogen bonding after water–silicon dioxide interaction [15]. Similarly, fracture mechanics measurements [34] have shown that precipitation of water-soluble silicates can support stress across solid silicate interfaces. Crack propagation in these *n*-pentanol vapor-exposed cantilever specimens provides good evidence that a low water content *n*-pentanol vapor environment was been attained in the current experiments.

When the separation or healing process is considered to be continuous, v–G curves are plotted, where v is the crack velocity. Because within experimental resolution the crack healing here is discrete in nature for most of the healing events [20], we shall characterize the results with $\bar{v} - G$ curves. Then the average crack healing velocity $\bar{v}$ is defined as

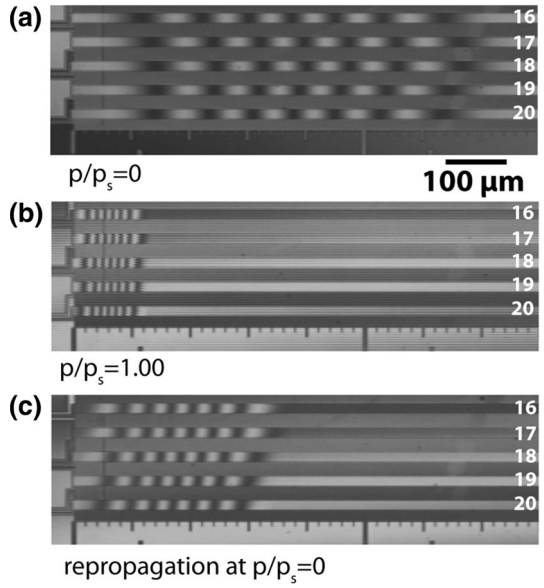

Fig. 3 Interferograms of crack lengths under dry ($p/p_s = 0$) **a**, fully saturated ($p/p_s = 1.0$) **b** and redried ($p/p_s = 0$) conditions **c**

$$\bar{v} = -\left(\frac{s_{j+n} - s_j}{\Delta t}\right). \tag{3}$$

Here, s_j is the crack length after j minutes, and s_{j+n} is a resolvable shorter crack length that occurs after $j + n$ minutes, and the "−" sign is used so that healing is a positive quantity. The time Δt is then n seconds. The G value is calculated at the average value of s, that is, at $s = (s_j + s_{j+n})/2$. The first $\bar{v}$ is calculated for a given microcantilever only after crack healing has initiated, i.e., $s_j < s_{\text{initial}}$.

Results reflecting 20 different cantilevers at $p/p_s = 0.3$, 0.5, 0.8, 0.9, and 0.95 are shown in Fig. 4. In each plot, $\bar{v}$ decreases from ~ 10 to $\sim 10^{-3}$ µm/s, which reflects the measurable crack velocity range in these experiments. Qualitatively, $\bar{v}$ decreases with G, because increasing crack opening force that develops as the crack heals becomes increasingly difficult to overcome. The highest energy release rate data points for each p/p_s condition are values close to the thresholds for crack healing and hence approach equilibrium. For $p/p_s = 0.3$, the G range is from 0.02 to 0.05 mJ/m^2, as shown in Fig. 4a. At the upper value of 0.05 mJ/m^2, the capillary closing force is no longer strong enough to promote further crack healing. At $p/p_s = 0.5$,G values range from 0.07 to 0.20 mJ/m^2, as plotted in Fig. 4b. At $p/p_s = 0.8$, G ranges from 0.07 to 0.98 mJ/m^2 as in Fig. 4c. At $p/p_s = 0.8$, the initial $\bar{v}$ is higher compared with other cases because the p/p_s increment (from 0.6 to 0.8) is high. In Fig. 4d, e, G values from 0.8 to 4.2 and 5.2 to 20.2 mJ/m^2 correspond to $p/p_s = 0.9$ and 0.95, respectively. Besides corresponding to increasing values of G for the same $\bar{v}$ range, Fig. 4a–e illustrates that the slope $|d[log(\bar{v})]/dG|$ decreases as p/p_s increases. Similar log-linear trends were observed in a previous study with water [20] (to compare with plots in e.g. refs. [10, 12] where crack healing is considered as negative, the data in Fig. 4 should be mirrored about the x-axis). Figure 5 plots the best fit slope $|d[log(\bar{v})]/dG|$ versus p/p_s for n-pentanol and water vapor.

In addition to the crack healing experiments with n-pentanol just described, we conducted experiments with water to compare Γ values in equilibrium. Here, equilibrium is taken to mean the G value after which no further crack healing was observed. It is seen that some crack healing events in Fig. 2 occurred near the end of the time at given p/p_s. This was noticed only after the experiment was analyzed in detail. Therefore, the Γ values should be taken as a reasonable estimate. The adhesion Γ is plotted against p/p_s in Fig. 6. The red square data markers are from five representative cantilevers in the n-pentanol experiment. Water vapor data are indicated by blue circle markers and were gathered from three different chips. One of the data sets presents data from three representative cantilevers at $p/p_s = 0.35$, 0.54, 0.66, 0.72, 0.77, 0.85, 0.92, 0.97 and 0.99. A second data set shows data from four representative cantilevers at $p/p_s = 0.34$, 0.54, 0.69, 0.80, 0.87, 0.95 and 1.00. Additionally, the data are displayed from five representative cantilevers at $p/p_s = 0.61$ and 0.88 taken from previous work [20]. The dashed lines in Fig. 6 are meant as a guide to the eye.

4 Discussion

4.1 Crack Healing Experiments

Under thermodynamic equilibrium, the value of r_K can be found from the Kelvin equation [35],

$$r_K = \frac{\gamma_{LV} V_m}{R_g T \ln(p/p_s)} \tag{4}$$

Here, r_K is the Kelvin radius, R_g is the ideal gas constant, T is temperature, p is the vapor pressure, p_s is the saturated vapor pressure, γ_{LV} is the surface tension at liquid–vapor interface, and V_m is the molar volume of the liquid substance. The Kelvin radius is at the nanometer scale over a wide range of p/p_s.

G extends to increasing values in Fig. 4. As p/p_s increases, $|r_K|$ increases, encouraging crack healing because capillary bridges can nucleate across larger gaps. The slope $|d[log(\bar{v})]/dG|$ in Fig. 4 is observed to be approximately constant at a given p/p_s, while at larger p/p_s, the slope decreases. These observations are similar to our previous study with water vapor [20] made at $RH = 0.605$ and 0.875. They now extend over a larger range from $p/p_s = 0.3$ to 0.95. The Fig. 4 $\bar{v}$ versus G data exhibit large scatter. This can be qualitatively explained by considering (a) that nucleation is a stochastic process and (b) that

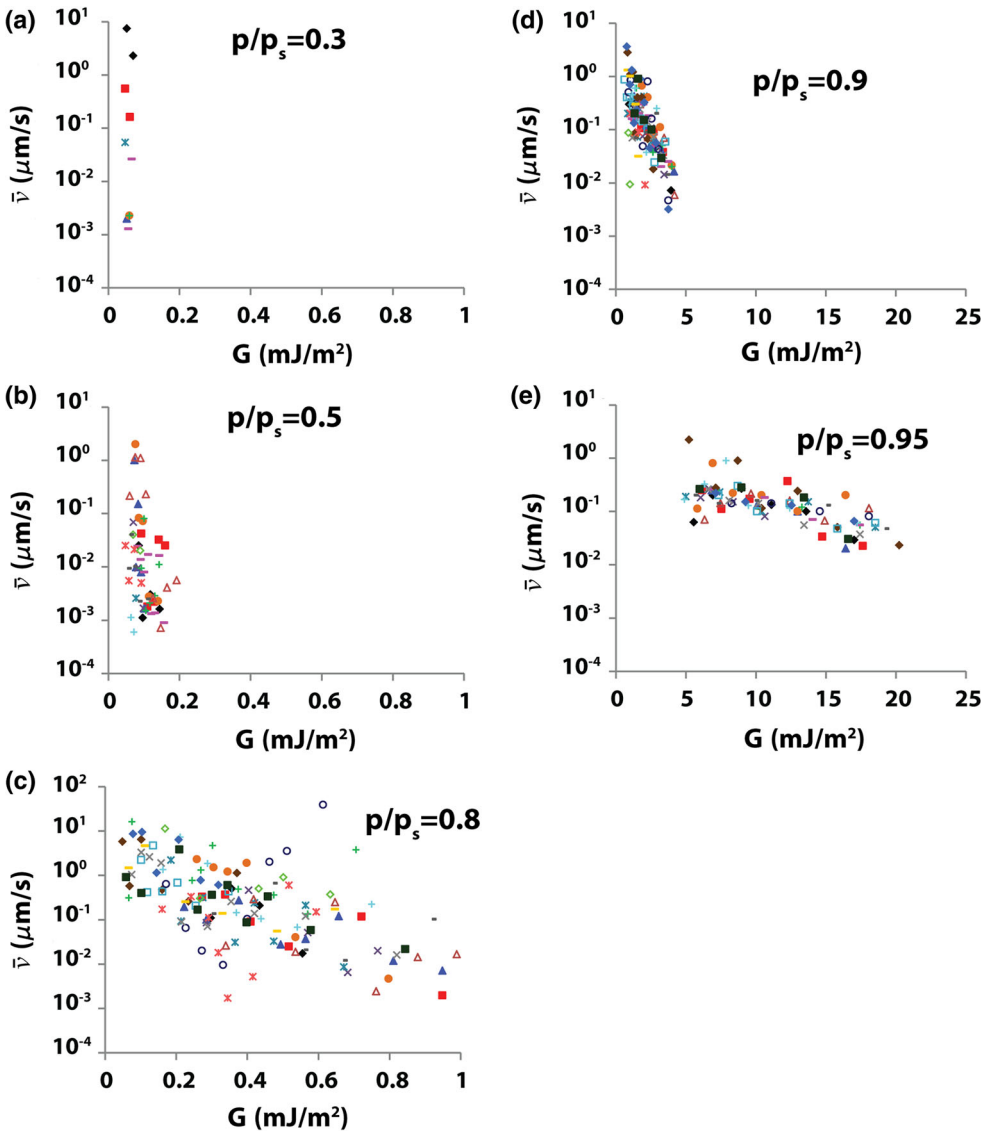

Fig. 4 Average crack healing velocity $\bar{v}$ as a function of energy release rate G in *n*-pentanol vapor. Different cantilever responses are plotted with *different color* and *marker* types. **a** $p/p_s = 0.3$, **b** $p/p_s = 0.5$, **c** $p/p_s = 0.8$, **d** $p/p_s = 0.9$, and **e** $p/p_s = 0.95$. The slope $|d[log(\bar{v})]/dG|$ decreases as p/p_s increases (Color figure online)

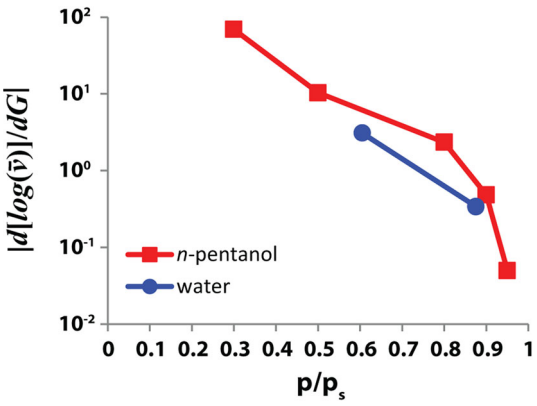

Fig. 5 $|d[log(\bar{v})]/dG|$ versus partial pressures of water and *n*-pentanol

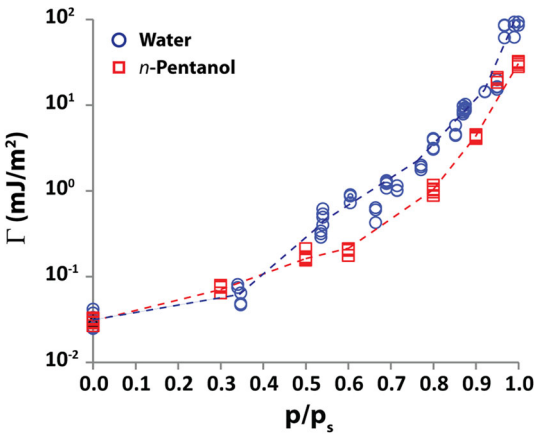

Fig. 6 Adhesion energy at equilibrium versus partial pressure data. Water and *n*-pentanol are represented by *blue circles* and *red squares*, respectively. The *dashed lines* are meant as a guide to the eye (Color figure online)

asperities encountered as the crack heals are at different heights. We have developed an extensive model that takes the surface roughness into account and achieves reasonable agreement with the crack healing rate data under wet conditions [36].

An important observation is that in Region I of the glass stress corrosion experiments [10, 11, 13] crack *propagation* velocity v_p increases with p/p_s at the same K, but the quantity $d[log(v_p)]/dK$ is independent of p/p_s. Because $G\alpha K^2$, $d[log(v_p)]/dG$ is also *independent* of p/p_s in the stress corrosion experiments, while $|d[log(\bar{v})]/dG|$ *depends strongly* on p/p_s in the present crack healing experiments. The difference in this characteristic feature is strong evidence that the underlying mechanisms are different. Indeed, the stress corrosion experiments are dominated by enhanced *chemical kinetics* at the crack tip, while the present crack healing experiments reflect *capillary bridge nucleation kinetics*.

The dependence of $|d[log(\bar{v})]/dG|$ on p/p_s for water and *n*-pentanol in Fig. 5 is similar, suggesting that the capillary bridge kinetics are strongly dependent on p/p_s. Capillary bridge nucleation requires exceeding an energy barrier, which depends theoretically on the ratio of the local asperity gap H to $2|r_K|$ [37]. The capillary bridge nucleation rate will increase with lower γ_{LV} and smaller $H/2|r_K|$. Comparing *n*-pentanol with water, γ_{LV} is smaller and $|r_K|$ is larger at the same p/p_s. This suggests that crack healing should be faster for *n*-pentanol if the surface separation is the same. However, as will be shown below, the work of adhesion for *n*-pentanol is smaller than water. Apparently, because a nucleated *n*-pentanol capillary bridge does less work in healing the crack than a nucleated water capillary bridge, the rates become roughly equal. It would be of interest to explore this balance in greater theoretical detail. The equivalence of the slopes is even more remarkable considering that compared with the $\bar{v}$ versus G data for *n*-pentanol, the data at the same p/p_s are shifted to higher G for water, as can be seen by comparing the data in Fig. 4d with Fig. 4 in Ref. [20].

4.2 Equilibrium Adhesion Experiments

The Kelvin Eq. (4) can be written as a coefficient divided by $\ln(p/p_s)$. This is done in Table 1 using the V_m and γ_{LV} values listed [38]. The resulting r_K coefficient, which depends on the product $\gamma_{LV}V_m$, is approximately a factor of two greater for *n*-pentanol than for water.

Table 1 Water, *n*-pentanol and ethanol properties

Substance	γ_{LV} (mN/m)	V_m (l/mol)	r_K coefficient (nm)
Water	0.073	0.018	0.53
n-Pentanol	0.026	0.108	1.15
Ethanol	0.023	0.058	0.54

For a sphere-flat geometry, with the assumption that the sphere radius $R \gg |r_K|$, the capillary force F_c versus sphere-flat separation H under thermodynamic equilibrium can be found from the Laplace and Kelvin equations as [39]

$$F_c = 4\pi R\gamma_{LV}\cos\theta\left[1 - \frac{H}{2|r_K|\cos\theta}\right]. \quad (5)$$

Here, θ is the contact angle between the meniscus and the surface. Given that each sample received an oxygen plasma cleaning, we take $\theta = 0$ in these experiments. This relation is plotted in Fig. 7 using solid lines for *n*-pentanol and water at $p/p_s = 0.6$, assuming $R = 100$ nm (a measured value, see following paragraphs). For $H = 0$, the maximum force F_c is limited by γ_{LV}. For $F_c = 0$, the maximum value of H extends to $2|r_K|$, which depends on the product $\gamma_{LV}V_m$ and is proportional to the r_K coefficient in Table 1. When the gap is greater than $2|r_K|$, the capillary bridge vanishes according to Eq. 5.

The existence of an adsorbed liquid layer, well known to be present on clean surfaces in vapor environments [40–42], clarifies how a liquid can bridge a gap H larger than $2|r_K|$ [43]. With $R \gg |r_K|$, this effect can be included in the capillary force–displacement equation as [44]:

$$F_c = 4\pi R\gamma_{LV}\left(1 + \frac{h_f}{|r_K|}\right)\cos\theta\left[1 - \frac{H}{2(|r_K| + h_f)\cos\theta}\right], \quad (6)$$

where h_f is the liquid film thickness. This relation is also plotted in Fig. 7 using dashed lines for *n*-pentanol and water at $p/p_s = 0.6$ assuming $R = 100$ nm. The adsorbed layer significantly increases both the maximum F_c and the

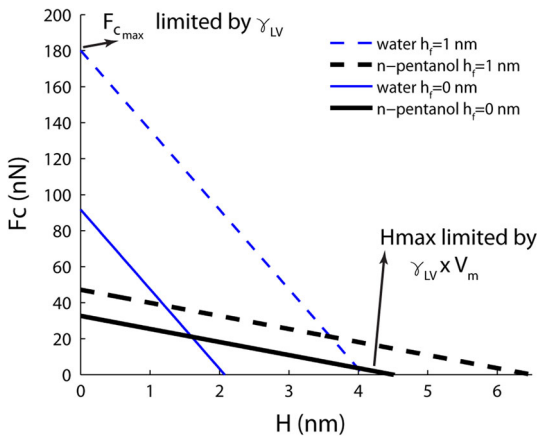

Fig. 7 Comparison of water and *n*-pentanol capillary forces (Eq. 5 and 6) as a function of H. Thin *blue lines* represent water, while thick *black lines* represent *n*-pentanol. $R = 100$ nm and $p/p_s = 0.6$ (Color figure online)

maximum H. The h_f values derive from adsorption isotherms, depend on p/p_s, and are taken from Refs. [40, 45] for n-pentanol and water, respectively.

The work of adhesion of an individual capillary bridge, W_c, corresponds to the area under the force–displacement curve. For $\theta = 0$,

$$W_c = 4\pi R\gamma_{LV}\left(1+\frac{h_f}{|r_K|}\right)\int_{H_0}^{2(|r_K|+h_f)}\left[1-\frac{H}{2(|r_K|+h_f)}\right]dH \tag{7}$$

where H_0 is the asperity-surface gap. If the gap is zero, this equation simplifies to

$$W_C = 4\pi R\gamma_{LV}(|r_K|+h_f) \tag{8}$$

The roughness of the multi-asperity surfaces in this work is on the order of $|r_K|$. Increasing roughness reduces capillary forces because the propensity for capillary bridging is reduced [46, 47]. We scanned the upper and lower counterfaces of the cantilevers using tapping mode AFM. As shown in Fig. 8, there are deep grain boundary grooves between the polysilicon grains that bias the operative roughness. These grooves do not play a role in capillary bridge nucleation, so only the intragrain roughness was characterized. The RMS roughness for the lower counterfaces was $\sim$1.4 and $\sim$1.8 nm for the water and n-pentanol samples, respectively. Similarly, the RMS roughness for the upper counterfaces was $\sim$1.7 and $\sim$1.8 nm for the water and n-pentanol samples, respectively. While there is a small difference, the surface character on a given counterface is qualitatively similar. Also, the dry condition adhesion values (Fig. 6 for $p/p_s = 0$) were nearly the same, and the cantilevers for both samples assumed the S-shape after the plasma cleaning. An effective asperity radius R_e of $\sim$100 nm was found by fitting the AFM topography data of the asperities into circular arcs [48] for the water, n-pentanol and ethanol samples. Given that multiple measures are similar, we assume that the surface roughnesses in the n-pentanol and water vapor experiments are equivalent.

For $0 < p/p_s \lesssim 0.5$, adhesion values in Fig. 6 for n-pentanol and water are roughly the same, whereas for $p/p_s \gtrsim 0.6$, the adhesion in n-pentanol is less than in water. A detailed analysis can be carried out, but is complex [19, 49]. Here, we seek to provide physical insight. For a given asperity gap H_0, the ratio of capillary adhesion in n-pentanol vapor, W_{cp}, to capillary adhesion in water vapor, W_{cW}, is

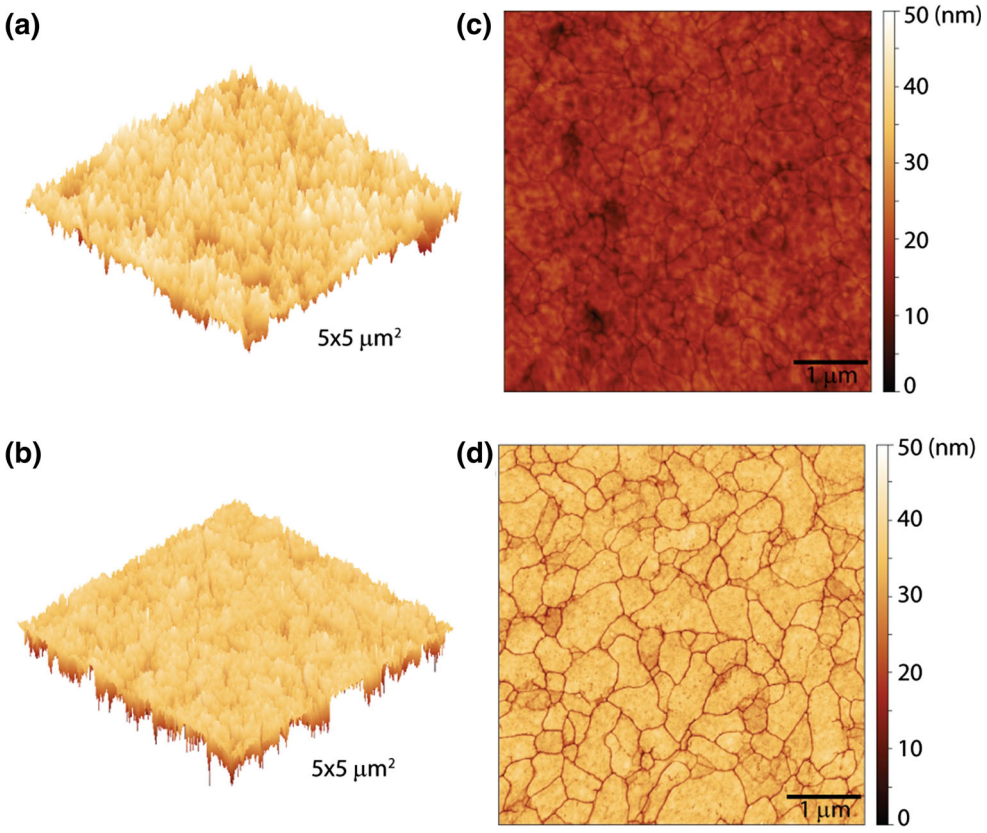

Fig. 8 AFM images of the upper **a**, **c** and lower **b**, **d** counterfaces of the n-pentanol experiment over 5 × 5 µm^2. **a**, **b** 3D data plot of the topography. **c**, **d** 2D data plot of the topography

$$W_{\text{ratio}} = \frac{W_{\text{Cp}}}{W_{\text{CW}}} = \frac{\left[\gamma_{\text{LV}}\left(1+\frac{h_{\text{f}}}{|r_{\text{K}}|}\right)\int_{H_0}^{2(|r_{\text{K}}|+h_{\text{f}})}\left[1-\frac{H}{2(|r_{\text{K}}|+h_{\text{f}})}\right]dH\right]_{\text{p}}}{\left[\gamma_{\text{LV}}\left(1+\frac{h_{\text{f}}}{|r_{\text{K}}|}\right)\int_{H_0}^{2(|r_{\text{K}}|+h_{\text{f}})}\left[1-\frac{H}{2(|r_{\text{K}}|+h_{\text{f}})}\right]dH\right]_{\text{W}}}. \quad (9)$$

The h_f values versus p/p_s are shown in Fig. 9a. They are taken from [40, 45], as measured and reported by the same authors. The ratio in Eq. (9) has been calculated in Fig. 9b for different values of H_0. For larger values of H_0, the ratio rapidly diverges as p/p_s decreases. This is because a liquid can bridge the asperity gap in *n*-pentanol vapor (i.e., $H_0 < [|r_K| + h_f]_p$), but not in water vapor (i.e., $H_0 > [|r_K| + h_f]_W$). In other words, the right side of the triangular shape in Fig. 7 still contributes to adhesion for *n*-pentanol, but not for water. As H_0 decreases, however, W_{ratio} remains less than one over a greater range of p/p_s. This is because the full triangle shape in Fig. 7 increasingly contributes to the adhesion.

Although the roughness of the surfaces is small, the real contact to apparent interface area is miniscule, likely less than 10^{-5} [19]. Therefore, capillary bridges that span gaps dominate the adhesion. There will be a large number of nonzero gaps per unit area for any given H_0 value. At low p/p_s, a significant number of gaps per unit area spanned by bridges in *n*-pentanol vapor may contribute strongly to the adhesion. These gaps cannot be spanned by bridges in water vapor. Hence, the adhesion in *n*-pentanol vapor approaches that in water vapor. For higher p/p_s values, larger gaps can be spanned in water. Furthermore, W_{ratio} becomes less than one, and hence, each capillary bridge contributes more to the adhesion. Thus, the adhesion in water vapor is greater than the adhesion in n-pentanol for $p/p_s \gtrsim 0.5$. Moreover, the adhesion in *n*-pentanol is approximately half that of water vapor. Hence, the value $W_{\text{ratio}} \approx 0.5$ is seen over a wide range of p/p_s in Fig. 6.

At $p/p_s = 0.95$, *n*-pentanol adhesion data in Fig. 6 are unexpectedly higher than water experiments results. A possible explanation is that the actual *n*-pentanol partial pressure is higher than 0.95. Because no partial pressure sensor was available for the alcohols, we controlled the flow meter mixing ratios by eye. This was reliable for low p/p_s, but at high p/p_s, r_K becomes very sensitive to small errors. For example, for a 1 % difference in p/p_s about 0.3, r_K changes by 0.03 nm, while for the same difference at $p/p_s = 0.95$, r_K changes by 5.75 nm for *n*-pentanol vapor. That is, a 1 % error in flow ratio imparts a negligible change at low p/p_s, but a significant change at higher values.

Data were also taken for ethanol vapor. In that case, no increase in adhesion was observed below $p/p_s \leq 0.8$. Finally, after increasing p/p_s to 0.9, adhesion began to rise, but remained approximately a factor of five below that in ethanol vapor. The chips that were used also exhibited small particles that reached well above the nominal roughness of the polysilicon, as seen in Fig. 10. These may be SiC particles, which grow due to residual carbon in the TEOS sacrificial layer [28, 50].

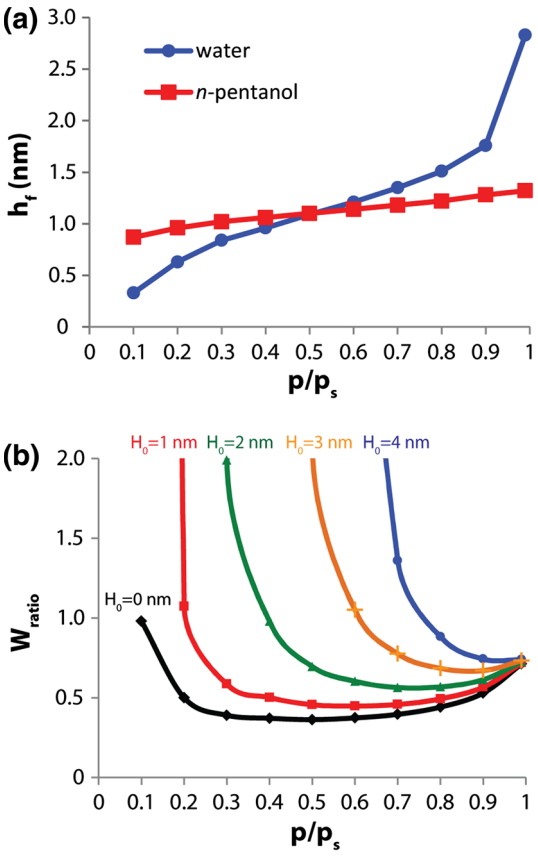

Fig. 9 **a** Adsorbed layer thickness as a function of p/p_s. Data from Refs. [40, 45], **b** Single asperity work of adhesion ratio of *n*-pentanol to water (Eq. 9) as a function of p/p_s for different asperity gaps

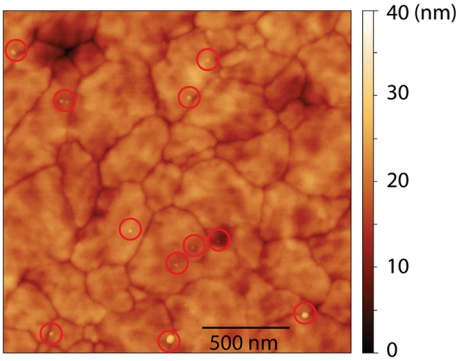

Fig. 10 AFM image of the upper counterface in the ethanol experiment sample over a 2x2 μm^2 area. *Red circles* indicate possible SiC particles (Color figure online)

We now wish to put the current work in perspective. An important motivation for studying alcohol-induced capillary adhesion is to help as a guide in applying vapor-phase lubrication in MEMS. This method immediately supplies lubricant through the gas phase to passivate contacting areas [51]. Recently, Kim, Dugger and colleagues have shown data indicating that alcohol-based vapors (ethanol through pentanol, i.e., C2–C5) provide effective wear prevention on a *microscale* MEMS tribology test structure made of polysilicon [6, 7]. These results extended from *nanoscale* oxidized Si asperities as measured by AFM to *macroscale* quartz (SiO_2) ball-on-flat linear wear tests in a conventional tribometer. The present work provides additional information on the adhesion energy of nano-scaled rough surfaces over a wide range of p/p_s in vapor environments. Minimizing the capillary adhesion will reduce forces to initiate sliding in a MEMS device. Also, knowledge of the kinetics of the capillary force development helps in the design of a cycling or rotating device. For example, at sufficiently high speeds, capillary bridges may not nucleate, and therefore, components may not encounter significant capillary adhesion.

Studies of measured friction coefficients on silicon surfaces using *n*-pentanol vapor-phase lubrication have been reported in Refs. [7, 52]. Asay et al. [7] used a MEMS sidewall friction technique at a nominal pressure of 20 MPa to measure the friction of a silane-coated surface with p/p_s varying from 0.08 to 0.95 in nitrogen carrier gas. This coating resulted in a 110° water contact angle that prevented capillary bridging due to water vapor. Ku et al. [52] used a MEMS tribometer at a nominal contact pressure of 8.47 kPa with no surface treatment but with saturated argon. Friction coefficients were $\approx$0.20 and $\approx$0.28 for the MEMS sidewall and tribometer experiments, respectively. The difference was attributed to dissimilarities in surface roughness and the presence of a silane monolayer-coating in the MEMS sidewall experiments [52]. The silane coating increases the water contact angle; it may also increase the contact angle of *n*-pentanol. Apparently, although the tribometer experiments encounter a lower apparent contact pressure, a higher friction coefficient was obtained due to *n*-pentanol capillary forces. This implies that the capillary forces we have studied in this paper may also have played a role in the tribometer experiments.

Previous measurements indicated that adhesion force increased as the number of cycles increased [6] for $p/p_s = 0.15$. This was attributed either to the rounding off of asperities, or to interfacial soft oligomer accumulation. Here, we find that except for very smooth surfaces, in the absence of sliding, the rate of adhesion increase is rather slow for contacting MEMS. For example, only a very small difference in roughness for the ethanol surfaces suppressed the effect of capillary action up to $p/p_s = 0.9$. Surfaces as smooth as those examined here (<2 nm RMS) are relatively uncommon for polycrystalline films. Therefore, we expect that vapor-phase lubrication can effectively prevent wear over a wide range of p/p_s for rougher MEMS interfaces. However, if a fixed amount of vapor is contained within a package, p/p_s increases rapidly as the temperature drops. For example, for water vapor, if $p/p_s = 0.5$ at 25 °C, it will increase to $p/p_s = 0.93$ at 15 °C, and hence, adhesion will increase rapidly [53]. Bulk liquid water condensation occurs at the dew point temperature of 13.9 °C. Hence, if temperature is not well controlled, capillary condensation will induce adhesion and may prevent sliding. Yet, if the vapor contains no water vapor, once the temperature rises, the adhesion may decrease again as indicated by Fig. 3c, and hence, the performance may be recovered.

5 Summary and Conclusions

Polysilicon microcantilever crack healing experiments were conducted in *n*-pentanol vapor at different partial pressures. A plot of crack healing velocity, $\bar{v}$, versus energy release rate, G, reveals log-linear behavior, while the slope $|d[log(\bar{v})]/dG|$ decreases with increasing p/p_s. The slopes are similar to water experiments when compared as a function of p/p_s. However, $|d[log(\bar{v})]/dG|$ decreases with p/p_s in crack healing experiments, while $d[log(v_p)]/dG$ is independent of p/p_s in glass stress corrosion experiments. This can be attributed to the different underlying mechanisms—nucleation kinetics in the former and chemical kinetics in the latter.

At low p/p_s, equilibrium adhesion values in *n*-pentanol and water vapor are approximately equivalent, while at higher $p/p_s > 0.5$, the adhesion in *n*-pentanol vapor is half that in water vapor. We rationalize these trends in terms of the larger *n*-pentanol Kelvin radius and liquid layer adsorption isotherms at low p/p_s and the greater work of adhesion of a water bridge at high p/p_s.

The cantilever response results presented here extend to a relatively low p/p_s of 0.3, where the Kelvin radii are 0.44 and 0.96 nm for water vapor and *n*-pentanol, respectively. To obtain the results, smooth surfaces were required. Here, the surface roughness of the top and bottom counterfaces was between 1.5 and 2.0 nm RMS. Cracks attained their shortest lengths when healed in vapor at $p/p_s = 1.0$, corresponding to $\Gamma \sim 30$ mJ/m^2. When p/p_s was subsequently reduced in *n*-pentanol vapor, the cracks propagated until the adhesion approached a relatively low level of $\sim$0.8 mJ/m^2. In comparison, in water vapor, adhesion reduces from $\sim$85 mJ/m^2 only to $\sim$80 mJ/m^2 after cracks have healed. This large difference may be attributed to the lower solubility of silica in *n*-pentanol compared with water.

Acknowledgments The authors gratefully acknowledge National Science Foundation funding through CMMI Grant No. CMMI 1030322. We also thank the technical staff in the Microelectronics Development Laboratory at Sandia National Labs in Albuquerque, NM, 87108 for fabricating the microcantilevers. We thank Professor W. Robert Ashurst for suggesting the use of the molecular sieves technique.

References

1. Mate, C.M.: Application of disjoining and capillary pressure to liquid lubricant films in magnetic recording. J. Appl. Phys. **72**, 3084 (1992)
2. Qian, J., Gao, H.: Scaling effects of wet adhesion in biological attachment systems. Acta Biomater. **2**, 51–58 (2006)
3. Mastrangelo, C.H., Hsu, C.H.: Mechanical stability and adhesion of microstructures under capillary forces-part I: basic theory. J. Microelectromech. Syst. **2**, 33–43 (1993)
4. Mastrangelo, C.H., Hsu, C.H.: Mechanical stability and adhesion of microstructures under capillary forces-part ii: experiments. J. Microelectromech. Syst. **2**, 44–55 (1993)
5. Sun, W., Neuzil, P., Kustandi, T.S., Oh, S., Samper, V.D.: The nature of the gecko lizard adhesive force. Biophys. J. **89**, L14–L17 (2005)
6. Asay, D.B., Dugger, M.T., Kim, S.H.: In-situ vapor-phase lubrication of MEMS. Tribol. Lett. **29**, 67–74 (2007)
7. Asay, D.B., Dugger, M.T., Ohlhausen, J.A., Kim, S.H.: Macro- to nanoscale wear prevention via molecular adsorption. Langmuir **24**, 155–159 (2008)
8. Barnette, A.L., Asay, D.B., Ohlhausen, J.A., Dugger, M.T., Kim, S.H.: Tribochemical polymerization of adsorbed n-pentanol on SiO2 during rubbing: when does it occur and is it responsible for effective vapor phase lubrication? Langmuir. **26**, 16299–16304 (2010)
9. Ma, J.: Advanced MEMS Technologies and Displays. Displays (2014)
10. Lawn, B.: Fracture of Brittle Solids. Cambridge University Press, Cambridge (1993)
11. Freiman, S.W., Wiederhorn, S.M., Mecholsky Jr, J.J.: Environmentally enhanced fracture of glass: a historical perspective. J. Am. Ceram. Soc. **92**, 1371–1382 (2009)
12. Wan, K., Aimard, N., Lathabai, S., Horn, R.G., Lawn, B.R.: Interfacial energy states of moisture-exposed cracks in mica. J. Mater. Res. **5**, 172–182 (1990)
13. Wiederhorn, S.M., Freiman, S.W., Fuller, E.R., Simmons, C.J.: Effects of water and other dielectrics on crack growth. J. Mater. Sci. **17**, 3460–3478 (1982)
14. Wondraczek, L., Dittmar, A., Oelgardt, C., Celarie, F., Ciccotti, M., Marliere, C.: Real-time observation of a non-equilibrium liquid condensate confined at tensile crack tips in oxide glasses. J. Am. Ceram. Soc. **89**, 746–749 (2006)
15. Michalske, T.A., Fuller, E.R.: Closure and repropagation of healed cracks in silicate glass. J. Am. Ceram. Soc. **68**, 586–590 (1985)
16. Wilson, B.A., Case, E.D.: In situ microscopy of crack healing in borosilicate glass. J. Mater. Sci. **32**, 3163–3175 (1997)
17. Holden, M.K.C., Frechette, V.D.: Healing of glass in humid environments. J. Am. Ceram. Soc. **72**, 2189–2193 (1989)
18. Lehman, R.L., Hill, R.E., Sigel, G.H.: Low-temperature crack closure in fluoride glass. J. Am. Ceram. Soc. **72**, 474–477 (1989)
19. De Boer, M.P.: Capillary adhesion between elastically hard rough surfaces. Exp. Mech. **47**, 171–183 (2007)
20. Soylemez, E., de Boer, M.P.: Capillary-induced crack healing between surfaces of nanoscale roughness. Langmuir **30**, 11625–11633 (2014)
21. Xue, X., Polycarpou, A.A., Phinney, L.M.: Measurement and modeling of adhesion energy between two rough microelectromechanical system (MEMS) surfaces. J. Adhes. Sci. Technol. **22**, 429–455 (2008)
22. Soylemez, E., de Boer, M.P., Ashurst, W.R.: Nucleation rate of capillary bridges between multi-asperity surfaces. MRS Proceedings, p. 1659. Cambridge University Press, Cambridge (2014)
23. Hariri, A., Zu, J.W., Mrad, R.: Ben: modeling of dry stiction in micro electro-mechanical systems (MEMS). J. Micromech. Microeng. **16**, 1195–1206 (2006)
24. Sniegowski, J.J., de Boer, M.P.: IC-compatible polysilicon surface micromachining. Annu. Rev. Mater. Sci. **30**, 299–333 (2000)
25. Meinhart, M., Miller, N., Saif, M.T.A.: Dry stiction of micro structures—theory and experiment. Proc. R. Soc. A Math. Phys. Eng. Sci. **462**, 567–585 (2006)
26. Soylemez, E., Plass, R.A., Ashurst, W.R., de Boer, M.P.: Probing microelectromechanical systems in an environmentally controlled chamber using long working distance interferometry. Rev. Sci. Instrum. **84**, 075006–1–075006–0750066 (2013)
27. De Boer, M.P., Michalske, T.A.: Accurate method for determining adhesion of cantilever beams. J. Appl. Phys. **86**, 817–827 (1999)
28. DelRio, F.W., Dunn, M.L., Boyce, B.L., Corwin, A.D., de Boer, M.P.: The effect of nanoparticles on rough surface adhesion. J. Appl. Phys. **99**, 104304 (2006)
29. DelRio, F.W., Dunn, M.L., Phinney, L.M., Bourdon, C.J., de Boer, M.P.: Rough surface adhesion in the presence of capillary condensation. Appl. Phys. Lett. **90**, 163104 (2007)
30. Williams, D.B.G., Lawton, M.: Drying of organic solvents: quantitative evaluation of the efficiency of several desiccants. J. Org. Chem. **75**, 8351–8354 (2010)
31. Greivenkamp, J.E., Bruning, J.H.: Optical Shop Testing. Wiley and Sons, New York (1992)
32. Jensen, B.D., Boer, M.P.De., Masters, N.D., Bitsie, F., Lavan, D.A.: Interferometry of actuated microcantilevers to determine material properties and test structure nonidealities in MEMS. J. Microelectromech. Syst. **10**, 336–346 (2001)
33. Delrio, F.W., de Boer, M.P., Knapp, J.A., David Reedy, E., Clews, P.J., Dunn, M.L.: The role of van der Waals forces in adhesion of micromachined surfaces. Nat. Mater. **4**, 629–634 (2005)
34. Bunker, B.C., Michalske, T.A.: Effect of surface corrosion on glass fracture. Springer, Boston, MA (1986)
35. Israelachvili, J.N.: Intermolecular and Surface Forces. Academic Press, Waltham (1992)
36. Soylemez, E.: Capillary kinetics between multi asperity surfaces. Ph.D. thesis, Carnegie Mellon University (2014)
37. Restagno, F., Bocquet, L., Biben, T.: Metastability and nucleation in capillary condensation. Phys. Rev. Lett. **84**, 2433–2436 (2000)
38. Yaws, C.L.: Yaws' Handbook of Thermodynamic and Physical Properties of Chemical Compounds. Knovel, New York (2003)
39. De Boer, M.P., de Boer, P.C.T.: Thermodynamics of capillary adhesion between rough surfaces. J. Colloid Interface Sci. **311**, 171–185 (2007)
40. Asay, D.B., Kim, S.H.: Evolution of the adsorbed water layer structure on silicon oxide at room temperature. J. Phys. Chem. B **109**, 16760–16763 (2005)
41. Wang, X., Zhao, M., Nolte, D.D.: Ambient molecular water accumulation on silica surfaces detected by a reflectance interference optical balance. Appl. Phys. Lett. **97**(183702–1), 183702–183703 (2010)
42. Theillet, P.-O., Pierron, O.N.: Quantifying adsorbed water monolayers on silicon MEMS resonators exposed to humid environments. Sensors Actuators A Phys. **171**, 375–380 (2011)
43. Christenson, H.K.: Phase behaviour in slits-when tight cracks stay wet. Colloids Surfaces A Physicochem. Eng. Asp. **124**, 355–367 (1997)

44. Mate, C.M., Lorenz, M.R., Novotny, V.J.: Atomic force microscopy of polymeric liquid films. J. Chem. Phys. **90**, 7550 (1989)
45. Asay, D.B., Kim, S.H.: Molar volume and adsorption isotherm dependence of capillary forces in nanoasperity contacts. Langmuir **23**, 12174–12178 (2007)
46. Butt, H.-J.: Capillary forces : influence of roughness and heterogeneity. Langmuir **24**, 4715–4721 (2008)
47. Rabinovich, Y.I., Adler, J.J., Esayanur, M.S., Ata, A., Singh, R.K., Moudgil, B.M.: Capillary forces between surfaces with nanoscale roughness. Adv. Colloid Interface Sci. **96**, 213–230 (2002)
48. Thoreson, E.J., Burnham, N.A.: Standard-deviation minimization for calibrating the radii of spheres attached to atomic force microscope cantilevers. Rev. Sci. Instrum. **75**, 1359–1362 (2004)
49. DelRio, F.W., Dunn, M.L., de Boer, M.P.: Capillary adhesion model for contacting micromachined surfaces. Scr. Mater. **59**, 916–920 (2008)
50. DelRio, F.W., Dunn, M.L., de Boer, M.P.: Growth of silicon carbide nanoparticles using tetraethylorthosilicate for microelectromechanical systems. Electrochem. Solid-State Lett. **10**, H27–H30 (2007)
51. Gellman, A.J.: Vapor lubricant transport in MEMS devices. Tribol. Lett. **17**, 455–461 (2004)
52. Ku, I.S.Y., Reddyhoff, T., Holmes, A.S., Spikes, H.A.: Wear of silicon surfaces in MEMS. Wear **271**, 1050–1058 (2011)
53. Dugger, M.T.: Tribological challenges in MEMS and their mitigation via vapor phase lubrication. SPIE Proc. **8031**, 80311H1–80311H–11 (2011)